Article

Real-time microscopy of the relaxation of a glass

Marta Ruiz-Ruiz[1,2], **Ana Vila-Costa** [1,2], **Tapas Bar** [2],
Cristian Rodríguez-Tinoco [1,2] ✉, **Marta Gonzalez-Silveira** [1,2],
Jose Antonio Plaza [3], **Jorge Alcalá** [4], **Jordi Fraxedas** [2] &
Javier Rodriguez-Viejo [1,2] ✉

The understanding of the dynamics of a glass above its devitrification temperature remains incomplete. Here, we build a spatio-temporal map of the relaxation dynamics of a highly stable glass into its supercooled liquid using real-time atomic force microscopy imaging. This methodology enables direct visualization of the progression of the liquid phase and clarifies and quantifies the presence of localized fast mobility regions separated by giant length scales. Our data establish a clear correlation between dynamic length and time scales in glasses. This approach may also be applicable to unveil the microscopic structure and dynamics of other glass-forming systems with much shorter length and time scales, including liquid-cooled glasses.

Glasses are non-equilibrium materials arrested during cooling in metastable configurations. The temperature that marks the transition from the ergodic state, the liquid, to the non-ergodic one, the glass, is known as the glass transition temperature, T_g. A hallmark in liquid and glassy dynamics is the recognition that dynamic heterogeneities are at the core of the slowing down of the dynamics and are responsible for the glass transition and its temperature dependence[1,2]. Dynamic heterogeneities are characterized by clusters of regions of atoms or molecules with correlated mobility that grow as the temperature is decreased. The existence of these clusters of mobility has been inferred from previous experiments[1,3–11], but it is experimentally challenging to identify them or their length scales, although it is recognized that the broad distribution of time scales in a glass can be associated with the presence of mobile and immobile regions[12,13]. It is generally accepted that the relaxation of the glass into the supercooled liquid (SCL) at the devitrification temperature on heating, T_{on}, happens through a gradual softening of the glass across its entire volume with a correlation length of a few nanometres. However, we have recently shown this view is not unique and can be changed by accessing a temperature and/or time regime above T_{on} where glasses transform into the liquid by the formation of localized regions of liquid within a glassy matrix[14], even

though the associated length scale has not been directly measured by experiments yet[15–17]. Vapour-deposited stable glasses appear as model systems to explore this scenario[18–21] and recent simulations point in this direction[22].

Since direct spatial visualization of equilibrated regions above T_{on} is extremely challenging due to the subtle structural changes over very small distances, we follow a different strategy based on the local mechanical instabilities that the liquid regions generate on a rigid ultrathin layer grown on top of the glass. Well-defined surface undulations can be produced in several ways[23,24], leading to self-organized wrinkling patterns with a rich variety of morphologies depending on the particularities of the system[25,26]. One approach to induce surface wrinkling is by capping a soft thin-film material (typically a polymer, but also a small-molecule organic glass) spin-coated on a rigid substrate by a thinner film of a metal layer[24] or by another organic layer with a higher T_g (ref. 27). The instability can be initiated by annealing the organic material into the rubbery state where wrinkling across the whole surface appears due to the development of compressive stresses induced by differences in thermal expansion coefficients[28,29]. Wrinkling can be locally induced at specific sites of the film by localized surface modifications using focused ion beams[30], swelling-induced

[1]Departament de Fisica, Facultat de Ciencies, Universitat Autonoma de Barcelona, Bellaterra, Barcelona, Spain. [2]Catalan Institute of Nanoscience and Nanotechnology (ICN2), CSIC and BIST, Campus UAB, Bellaterra, Barcelona, Spain. [3]Instituto de Microelectrónica de Barcelona, IMB-CNM (CSIC), Campus UAB, Bellaterra, Barcelona, Spain. [4]InSup, ETSEIB, Polytechnic University of Catalonia, Barcelona, Spain. ✉e-mail: cristian.rodriguez@uab.cat; javier.rodriguez@uab.cat
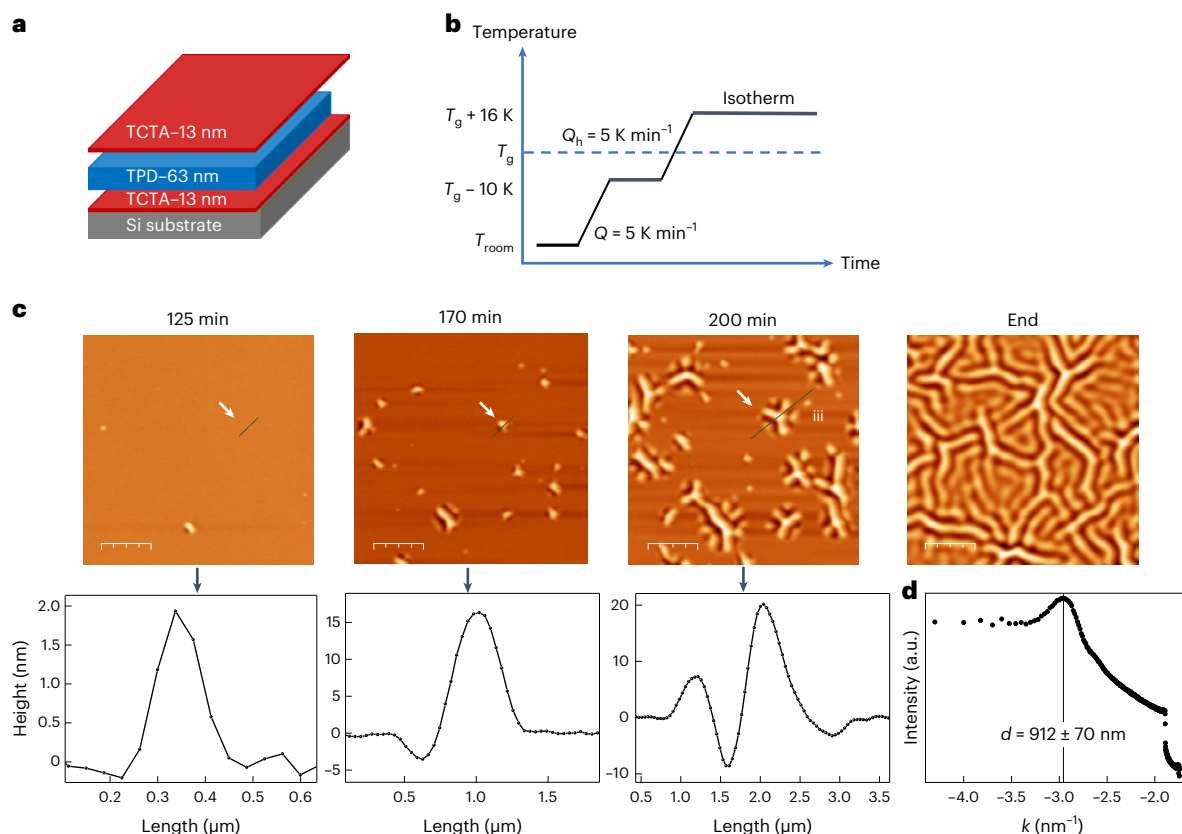
Fig. 1 | Representative images of the highly heterogeneous transformation of a stable TPD glass. a,b, Sketch of the trilayer structure (**a**) and of the annealing protocol (**b**) in the AFM setup. **c**, AFM snapshots obtained at 349 K after time t showing the formation and progression of local wrinkles induced by the transformation of the middle TPD layer into a SCL. The bottom graphs show the line profiles of the selected regions. A white arrow marks the pattern considered. Scale bars, 4.0 μm. **d**, Power spectral density (PSD) distribution of the fully transformed sample indicating the prominent wavelength of the wrinkled distribution. PSD has been calculated with WxSM software with no associated uncertainty. The value of d is determined from the maximum of PSD with an error corresponding to the separation between two adjacent points.

stress through toluene absorption[31] or local heating with an external source, such as a laser[32].

Here, we take advantage of a previously established protocol to induce bulk 'melting' in thin-film glasses[33–35] by capping the organic film (N,N'-bis(3-methylphenyl)-N,N'-diphenylbenzidinem, TPD, T_{g1} = 333 K measured at 10 K min^{-1}) with two ultrathin layers of an organic glass with a higher T_g (tris(4-carbazoyl-9-ylphenyl)amine or TCTA, T_{g2} = 428 K, 10 K min^{-1}). The mechanical instabilities produced during isothermal treatments above T_{g1} are measured in situ using atomic force microscopy (AFM) and optical microscopy. We address the continuum mechanics finite element modelling (FEM) of the wrinkling phenomenon to demonstrate that the local surface wrinkles appearing at $T_{ann} > T_{g1}$ (TPD) are induced by the equilibration of the intermediate TPD layer at localized spots. The observed patterns are compatible with a time-dependent number of initiation sites that appear to propagate radially. With these data, we construct a spatio-temporal, microscopic map of the relaxation of a molecular glass, delivering a clear picture of the heterogeneous devitrification dynamics of glasses with enhanced stability. Imaging by AFM or optical microscopy provides a direct visualization of giant lengths scales between fast mobility regions and the growth of the liquid by dynamic facilitation. This methodology also offers an original approach to study the glass transition from a localized and new perspective and bridge the gap with the microscopic information accessible to computer simulations[13,22,36].

A sketch of the trilayer organic structure grown on a 500-μm-thick Si substrate with its native oxide (surface root mean square (RMS) roughness, 0.13 nm in 1×1 μm^2) together with the thermal protocol

is shown in Fig. 1a,b. The TPD layer is vapour-deposited at a substrate temperature of $0.85T_{g1}$ (285 K) and has a fictive temperature[37], T_f = 292 ± 2 K, 40 K below its T_{g1}. Details of the growth of the organic layers and the experiments are given in the Methods. After growth, the thin-film stack (13 nm TCTA/63 nm TPD/13 nm TCTA/silicon, Fig. 1a) is taken to an AFM or optical microscope equipped with a heating stage. Most results involve AFM due to its superior spatial resolution. In AFM, the temperature is raised to a working value of 349 K, T_{g1} + 16 K, in sequential steps as shown in Fig. 1b to allow for equilibration of the AFM setup (Methods). At 349 ± 1 K, the transformation time of TPD into the SCL is around 270 min ($t_{trans} \cong 2 \times 10^6 \tau_\alpha$, where τ_α is the relaxation time of the equilibrated liquid at that temperature)[38], taking t = 0 s as the time at which this temperature is reached. This time interval offers a convenient scale to follow the kinetics of the transformation in real time, given that each AFM scan takes around 4 min to complete (Methods). Figure 1c shows some representative in situ AFM images obtained at $T = T_{g1}$ + 16 K in the same spatial location for different times. The surface of the trilayer was initially very smooth (RMS roughness below 0.3 nm in 1×1 μm^2) and did not show any surface undulation before reaching the annealing temperature. Figure 1c bottom represents the apparent height of the surface topography across the line scans marked in the AFM images (Methods). The images reveal the emergence of surface corrugation that initially appears in the form of Gaussian-type protuberances with aspect ratios around 100:1, that is, a few nanometres in height and a few hundred nanometres in width. The corrugation develops over time so as to form localized wrinkle patterns that grow radially from the initial seed. A set of AFM and optical
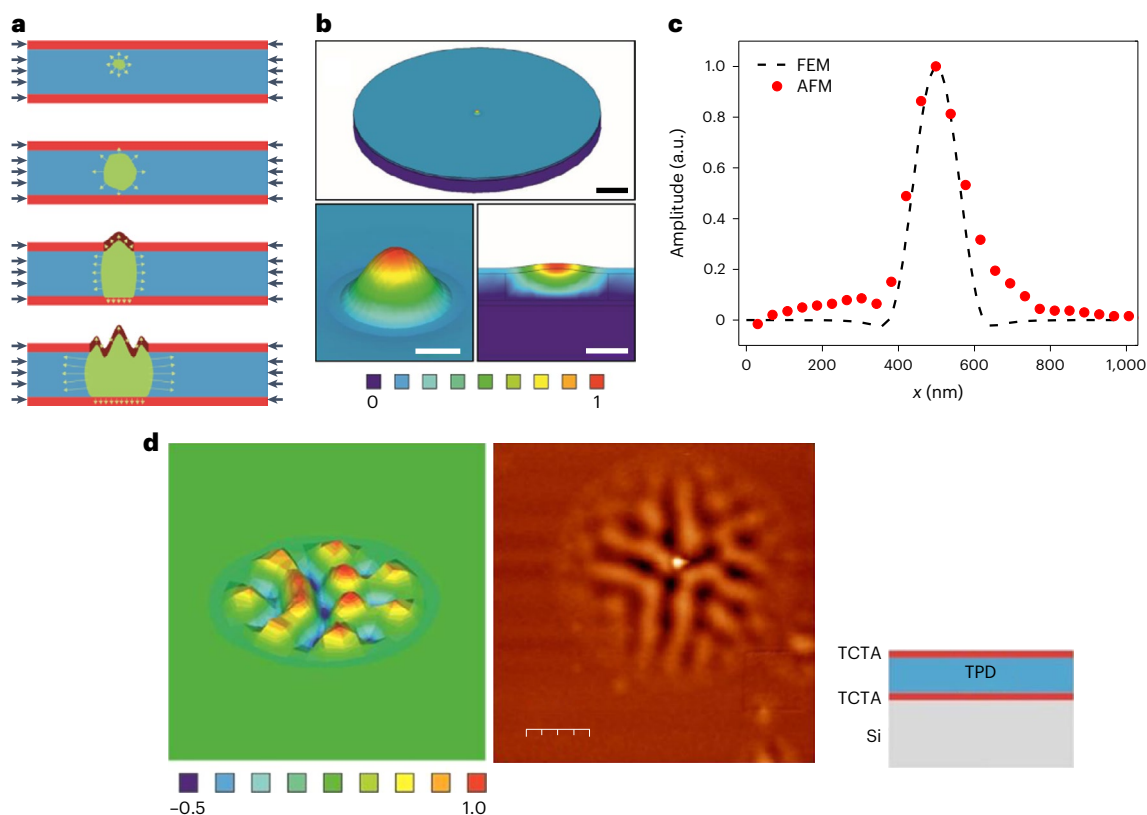
Fig. 2 | Surface undulation patterns and their modelling via finite element simulations. a, Schematic showing the growth of an SCL region (in green) from a nucleation site within the TPD interlayer towards the top and bottom TCTA layers (growth direction marked with green arrows). This results in the development of the first surface undulation triggered under the applied thermal stresses (marked with black arrows). Notice the periodic onset of further secondary undulations as the cylindrical-shaped SCL region extends radially and mechanical instabilities develop. **b**, Simulated normalized out-of-plane displacement (top) isotropic view of the whole simulated structure, (bottom, left) isotropic view of a zoomed region containing the first surface undulation of diameter $\theta \cong 250$ nm within the TPD interlayer and (bottom, right) a cross-sectional view of the surface undulation region. The neo-Hookean model with material parameters $C = 3.71 \times 10^6$ Pa and $d = 5.58 \times 10^{-8}$ Pa^{-1} is assumed in the simulations. **c**, Comparison between the simulation results from finite element modelling (FEM) and the experimental AFM measurements concerning the shape of the first undulation during the early propagation stages of the liquified front. AFM data is for an emerging liquid nucleus, with no associated uncertainty values. **d**, Comparison between a simulated wrinkled pattern of $\theta \cong 1,000$ nm under the assumption of the neo-Hookean model with material parameters $C = 3.71 \times 10^6$ Pa and $d = 5.58 \times 10^{-8}$ Pa^{-1}, and the AFM image of a typical pattern in 13/63/13 nm trilayers. Scale bars, 1.2 μm.

microscopy images of the transformation of a 13/63/13 nm trilayer are shown as videos in Supplementary Videos 1 and 2. We note that the onset of the local perturbations could not be identified by AFM, so these measurements are not sensitive to the initial formation of the liquid droplet within the film and only monitor its appearance when the liquid region is larger than the thickness of the middle layer (schematics in Fig. 2a). This limits the spatial resolution to the thickness of this layer. The peak-to-peak amplitude of the central part evolves from 2 to 3 nm of the initial seeds to around roughly 30 nm (peak-to-valley) at the end (Fig. 1c), although the precise dimensions depend slightly on the selected wrinkled pattern. The dominant wavelength of the fully transformed sample, obtained from the power spectrum analysis of the fast Fourier transform image, Fig. 1d, amounts to 912 nm (Methods). The AFM images in Fig. 1 and Supplementary Videos 1 and 2 show two main features: the appearance of new local corrugations of the trilayer as time evolves and their radial growth. Corrugation is irreversible and maintains its structure over months at room temperature. The observed patterns are not associated with crystallization, grazing-incidence X-ray diffraction as well as transmission electron microscopy imaging of the fully corrugated sample after the thermal treatment show that the trilayer maintains its amorphous structure (Supplementary Fig. 1). Capping the TPD middle layer at both sides is required to avoid surface induced transformation and to observe

localized patterns evolving with time. TPD samples grown directly on weakly interacting native oxide–Si substrates and capped only on top by TCTA do show wrinkling at the whole surface from the beginning of the experiment due to the transformation of TPD into the SCL by a propagation front that starts at the TPD–SiO$_2$ interface (Supplementary Fig. 2). This corrugation behaviour is consistent with the thermal wrinkling commonly observed in metal and polymer bilayers[39].

Mechanical analysis of wrinkle formation

Continuum mechanics finite element simulations are used to correlate the formation of surface undulations with the existence of SCL regions within the intermediate TPD layer. A distinctive feature of the investigated mechanical instabilities compared with most previous thermal wrinkling studies is their local character, where the softened (liquid) sites slowly populate the interlayer. While the three-layer thin-film system thus behaves in accordance with linear thermoelasticity, cylindrical SCL regions arise in the middle TPD layer after some time above T_{g1}. Surface undulation patterns are then induced due to the transfer of the compressive thermal loads from the TPD interlayer to the stiffer and much thinner TCTA top layer, which remains in its glassy state. This is a mechanically unstable phenomenon triggered under the roughly 33-fold higher elastic modulus and roughly 88-fold smaller thermal expansion coefficient of the Si substrate compared to the organic

layers. These surface undulation processes are schematically illustrated in Fig. 2a, resulting in the experimentally observed wrinkled patterns. Concentrically ridged undulations are also produced as a function of the relative layer thicknesses (Supplementary Fig. 3).

The onset of the first surface undulation (single ridge configuration) is concomitant to the vertical expansion of the cylindrical SCL regions due to density (ρ) differences between the liquid and the ultrastable glass (UG) (ρ(UG) 2.8% higher than ρ(SCL) at T_{g1} + 16 K (refs. 40,41) and the compression induced by the surrounding TPD glassy interlayer. The capacity of the cylindrical SCL regions to withstand shear stresses at the outermost regions close to the top TCTA layer is then regarded as an essential element of the attainment of the multiple periodic undulations associated with the mechanical instability of the thin-film system. The sudden inception of fully wrinkled surfaces with the partly capped, two-layer system (Supplementary Fig. 2) is indicative in that this capacity is maintained across larger surface areas. Some viscous relaxation of the shear stresses is finally seen to occur at T_{g1} + 16 K, tentatively reducing the heights of the undulations.

In our finite element simulations, we consider that the softened TPD interlayer is a dense liquid that exhibits solid-like properties below a certain elastic limit. As we are essentially interested in assessing the onset of the surface undulations under sustained shear, it is assumed that the cylindrical SCL regions deform though linear elasticity with discretionary levels of compressibility and small elastic modulus. The softened interlayer is alternatively assumed to deform under the non-linear neo-Hookean hyperelastic model, so as to capture a possible decrease in the initial elastic modulus at small strain levels (Methods). Comparisons between the experimental and computational results are shown in Fig. 2b–d. A cross-section of a scanning electron micrograph showing the surface undulation of a trilayer is shown in Supplementary Fig. 8b.

Equilibration of liquid regions: giant length scales

The images of Fig. 1c and Supplementary Videos 1 and 2 offer a detailed view of the evolution of the glass following a temperature jump above T_{g1}, in which localized regions within the TPD glass having higher mobilities evolve towards the liquid state: a process referred to as softening and equilibration, subsequently consuming the glassy environment by dynamic facilitation. These images clarify previous experiments and theories about the bulk transformation of stable glasses[18–20,42]. These studies, through indirect measurements, suggested that bulk melting on these glasses proceeds through a 'nucleation and growth'-type process with giant length scales between the initial patches of liquid. Here, we assume the first regions equilibrating into the liquid correspond to those with the highest mobility and therefore we interpret the emergence of newly equilibrated regions at different times as clear evidence of dynamic heterogeneity. Our results confirm that dynamic heterogeneities in UGs are characterized by giant length scales of many micrometres between fast mobility regions. Besides these localized spots, we also have indirect evidence that the entire glass matrix slowly softens during the annealing above T_{g1}, but to the most part without reaching equilibration. Calorimetric measurements show the change in the position of the endothermic overshoot of the highly stable glass matrix during the annealing treatment (ref. 17 and Supplementary Fig. 4).

In Fig. 3, we represent the time evolution of the heterogeneous, localized softening obtained from AFM. Figure 3a plots the cumulative number of regions that enter the regime of equilibration and become liquid-like per unit area (black symbols). The inset is a plot of the newly developed liquid regions per unit area (black circles), and normalized by the area of the untransformed fraction (blue symbols) as a function of time (Supplementary Information). This representation highlights an acceleration of the number of local regions entering the liquid regime over time. We foresee two possible scenarios to explain this behaviour: (1) acceleration originates from the softening of the matrix,

or (2) it is directly related to the intrinsic shape of the distribution of relaxation times of the UG at this temperature, or to some mixed effect. In Fig. 3b we plot a two-dimensional spatial map of the sample with the position of the equilibration spots as they appear. The colour scale marks the time from the appearance of the first liquid regions.

An initial period of about 2 h without any noticeable surface feature can be clearly discerned in Fig. 3a. This long transient is related to the high stability of the glass, that is, some regions attain liquid mobility within this long time. To some extent, the large induction period could also be associated to a slower growth velocity of the minuscule initial seeds localized inside the TPD matrix before they reach the TCTA capping layers due to pressure effects originating from density differences between the UG and the SCL above T_{g1}, as reported recently in a numerical simulation study[22]. This effect may have a minor influence here because of the small layer thickness but could become important for thicker films. In the time interval between 0.9 and 1.25×10^4 s, the evolution of the number of liquid seeds (Fig. 3a) can be roughly approximated by a linear function (dashed blue line in Fig. 3a) giving an average 'formation frequency' $v \cong 6 \pm 2 \times 10^7$ nuclei m^{-2} s^{-1}. This magnitude translates into a mean separation distance of liquid droplets appearing in 1 s per unit area of $\cong$130 µm, using $\xi(T) = (v(1s))^{-1/d}$, where d is the dimensionality of the system. Experimentally, the giant length scale of the bulk transformation was previously indirectly inferred from the lower bound of the cross-over length between front propagation and bulk melting, as well as from calorimetric measurements that identified the appearance of isolated liquid regions[15,16]. Length scales of the order of 1–4 µm have been suggested. To compare with previous estimates of the cross-over length in thin films, it is necessary to account for the time dependence. That is, in 3,000 s the average distance between localized liquid regions roughly equals 2 µm (under the assumed $v = 6 \times 10^7$ nuclei m^{-2} s^{-1} (Fig. 3a)), which falls within the same order of magnitude as the roughly 1.2 µm distance travelled by the front at T_{g1} + 16 K in the same time scale (considering $v_{\text{front}} \cong 0.4$ nm s^{-1}, as discussed below). This confirms the length scale from the previous cross-over experiments[15,16].

Relaxation map of the glass

We also follow the time evolution of the size of the liquid regions both from AFM and optical microscopy images (Fig. 4 and Supplementary Fig. 5). The methodology used to extract the radius of the liquid domains and the transformed fraction of liquid from the AFM and optical microscopy images is described in detail in the text accompanying Supplementary Figs. 12 and 13. A strong indicator that the wrinkles originate from the presence of liquid in the TPD layer is found in the radial propagation velocity of the instability region. We have analysed many individual spots, such as those shown in Fig. 4a, rendering an average radial propagation speed at T_{g1} + (16 ± 1) K of 0.3 ± 0.1 nm s^{-1}. This is consistent with the growth front velocity of the SCL TPD at this temperature, $v = 0.4 \pm 0.1$ nm s^{-1}, evaluated independently through extrapolation of high and low-temperature calorimetric data (Supplementary Fig. 6). Thus, the wrinkle patterns propagate laterally at the speed of the liquid front, confirming a previous hypothesis[17]. Although the liquid signature on the mechanical instability looks radial on average, we cannot infer whether mobility locally spreads isotropically or through string-like, fractal, dynamics. From the wrinkled area, we can estimate the liquid transformed fraction (Supplementary Fig. 13) that follows a sharp sigmoidal shape, as shown in Fig. 4b, most probably due to the continuous formation of new liquid seeds and its acceleration as time evolves. Figure 4c,d represents spatio-temporal maps of the evolution of the liquid including its progression by dynamic facilitation taken at transformed liquid fractions X = 34 and 90%, respectively, and can be interpreted as relaxation maps of the glass. As time progresses, regions of fast mobility spatially separated by giant length scales equilibrate towards the liquid and they ignite adjacent regions that also become more mobile by a facilitation mechanism. A direct comparison between
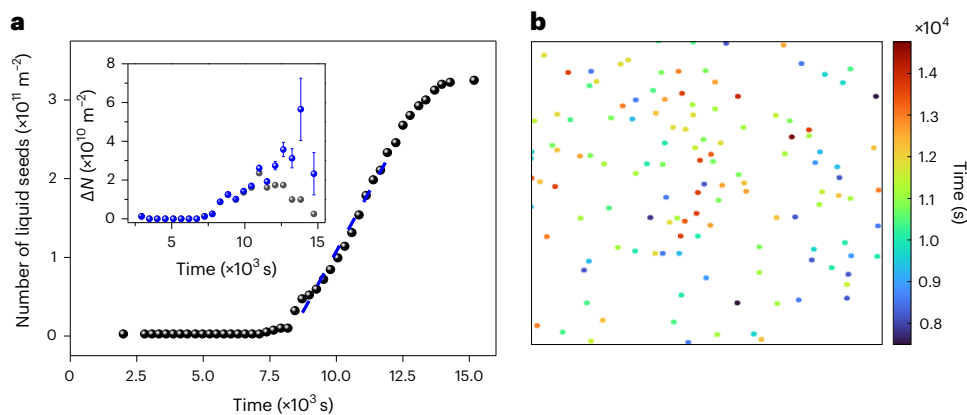
Fig. 3 | Formation of liquid seeds in the TPD interlayer during annealing above T_g. a, Evolution of the cumulative number of nuclei per unit area. No uncertainty is considered for the absolute discrete number of nuclei. The inset shows a number of new nuclei that appear in each AFM image per unit area (black symbols) and per unit area of untransformed glass (blue symbols). The error bars in the inset is propagated from the error in the calculation of the transformed fraction (Fig. 4b). **b,** A spatial map at 90% of transformation obtained from AFM images showing mobility regions where glass relaxes directly into the liquid. The colour code reflects the time of formation; $t = 0$ marks the time at which the temperature reaches 349 K. The first soft spots appear after 2 h.
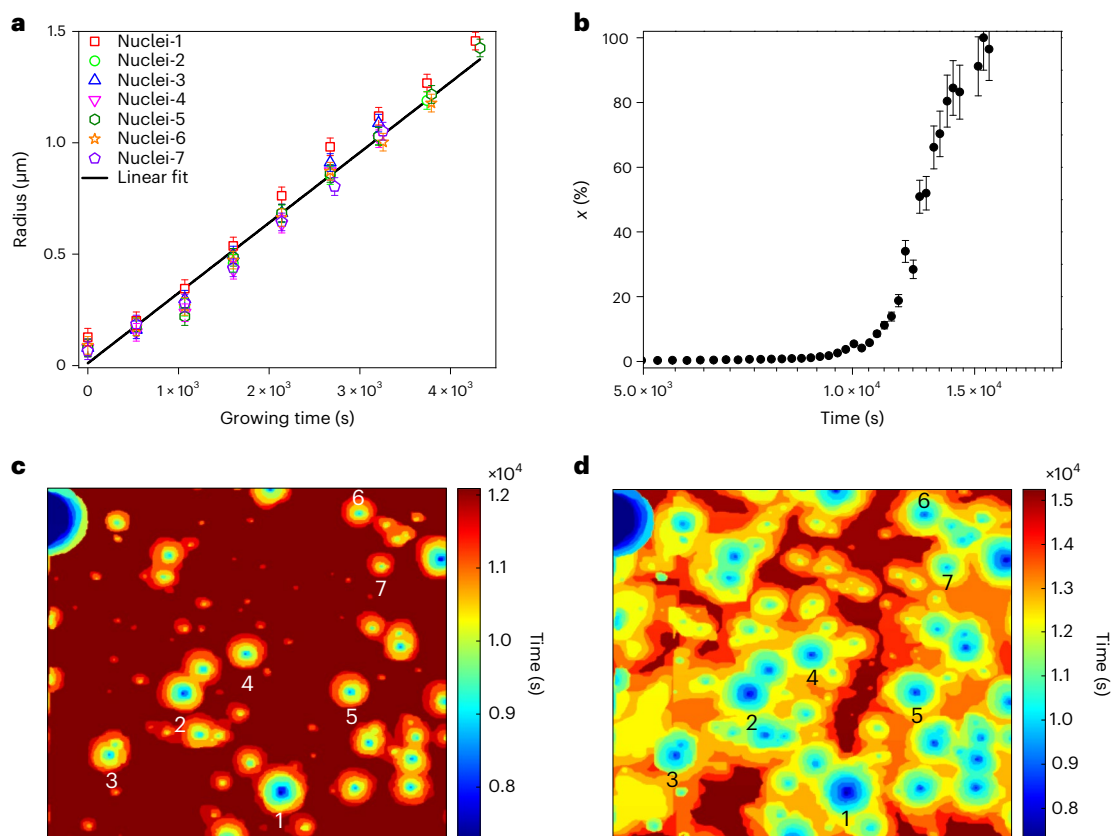

Fig. 4 | Relaxation maps of the stable TPD glass showing the impact of dynamic facilitation. a, Growth of several liquid regions as a function of time at $T_{g1} + 16$ K. The growth time is normalized with respect to the observed nucleation time for each nucleus. The radius of the SCL regions represent best fit values to the AFM images. The error bars range between the smallest and largest circles that could fit at least some of the points of the perimeter of the liquid regions, as shown in Supplementary Fig. 12. **b,** Transformed fraction of liquid versus time. Data points correspond to the total liquid area calculated as explained in the Supplementary Information. The error bars show an uncertainty proportional to the total length of the perimeter of the liquid regions, and are thus considered to be 10% of the transformed fraction. **c,d,** Spatio-temporal maps of the relaxation of the glass including lateral progression of the liquid by dynamic facilitation at 34% (**c**) and 90% (**d**) of transformed fraction. The colour scale marks the time evolution. The nuclei evaluated in **a** are indicated by numbers.

the maps at 90% of the transformation of Figs. 3b and 4d evidence that most of the glass transforms into liquid by dynamic facilitation, suggesting that a large fraction of the as-prepared glass consists of highly stable, inactive regions that may only transform from adjacent zones that have become liquid. Roughly 10–15% of the glass has still not transformed after 1.5×10^4 s at $T_{g1} + 16$ K (darker brown areas in Fig. 4d),

indicating that these regions show relaxation times above roughly $2 \times 10^6 \tau_\alpha$. The mechanism described above is consistent across a range of annealing temperatures above T_{g1} and thickness of the TPD layers (60–400 nm), as briefly shown in Supplementary Figs. 7–9 and 11, but we leave a complete study for future work. We emphasize trilayers grown on clean and smooth surfaces transform by a 'bulk-like' process that is not influenced by interfaces in the thickness range analysed here, in agreement with previous measurements[33,43]. The onset temperature of formation of the liquid regions is the same, $T_{on} = 79.5 \pm 0.5\,°C$, for both 13/63/13 and 13/200/13 trilayers, as demonstrated during in operando AFM and/or optical microscopy measurements under slow heating rates of 0.1 K min^{-1} (Supplementary Fig. 9). This value also agrees with the T_{on} estimated from differential scanning calorimetry data at 0.1 K min^{-1} ($T_{on} = 79.5 \pm 0.5\,°C$) on a bulk, 20-µm-thick sample vapour-deposited at $0.85T_g$. (Supplementary Fig. 9, right). We also note in passing that the dynamics can be accelerated by the presence of defects or contamination on the substrate surface before vapour deposition (or increased roughness of the substrate) as shown in Supplementary Figs. 10 and 11.

Conclusions and outlook

We have reported a clear, direct and real-time visualization of the spatio-temporal dynamics of the devitrification of an ultrastable glass by AFM and optical measurements. Our data unambiguously demonstrate the correlation between time and length scales in glasses. Glasses with ultraslow average dynamics and huge transformation times, $\tau_{glass} \cong 10^6 \tau_\alpha$, show giant length scales, measured as the average distance between patches of fast mobility that equilibrate into the liquid, of the order of 100 µm at $T_{g1} + 16$ K. This giant length scale paves the way to manipulate the properties of ultrastable glasses by nanostructuration, opening an interesting avenue to further influence the dynamics. We also anticipate that reducing the stability of the glass (that is, its time scale) will also result in a reduction of the length scale. By using the mechanical instabilities described here, it should be possible to test the existence of heterogeneity on a smaller time and spatial scale by using ultrathin capped layers in less-stable glasses, ultimately enabling a quasi-direct observation of dynamic heterogeneities in liquid-cooled glasses.

Online content

Any methods, additional references, Nature Portfolio reporting summaries, source data, extended data, supplementary information, acknowledgements, peer review information; details of author contributions and competing interests; and statements of data and code availability are available at https://doi.org/10.1038/s41567-023-02125-0.

References

1. Ediger, M. D. Spatially heterogeneous dynamics in supercooled liquids. *Annu. Rev. Phys. Chem.* **51**, 99–128 (2000).
2. Karmakar, S., Dasgupta, C. & Sastry, S. Growing length scales and their relation to timescales in glass-forming liquids. *Annu. Rev. Condens. Matter Phys.* **5**, 255–284 (2014).
3. Sillescu, H. Heterogeneity at the glass transition: a review. *J. Non Cryst. Solids* **243**, 81–108 (1999).
4. Richert, R. Heterogeneous dynamics in liquids: fluctuations in space and time. *J. Phys. Condens. Matter* **14**, 201 (2002).
5. Vidal Russell, E. & Israeloff, N. E. Direct observation of molecular cooperativity near the glass transition. *Nature* **408**, 695–698 (2000).
6. Schiener, B., Böhmer, R., Loidl, A. & Chamberlin, R. V. Nonresonant spectral hole burning in the slow dielectric response of supercooled liquids. *Science* **274**, 752–754 (1996).
7. Zondervan, R., Kulzer, F., Berkhout, G. C. G. & Orrit, M. Local viscosity of supercooled glycerol near T_g probed by rotational diffusion of ensembles and single dye molecules. *Proc. Natl Acad. Sci. USA* **104**, 12628–12633 (2007).
8. Cicerone, M. T., Zhong, Q. & Tyagi, M. Picosecond dynamic heterogeneity, hopping, and Johari-Goldstein relaxation in glass-forming liquids. *Phys. Rev. Lett.* **113**, 117801 (2014).
9. Caporaletti, F. et al. Experimental evidence of mosaic structure in strongly supercooled molecular liquids. *Nat. Commun.* **12**, 1867 (2021).
10. Paeng, K., Park, H., Hoang, D. T. & Kaufman, L. J. Ideal probe single-molecule experiments reveal the intrinsic dynamic heterogeneity of a supercooled liquid. *Proc. Natl Acad. Sci. USA* **112**, 4952–4957 (2015).
11. Zhang, P., Maldonis, J. J., Liu, Z., Schroers, J. & Voyles, P. M. Spatially heterogeneous dynamics in a metallic glass forming liquid imaged by electron correlation microscopy. *Nat. Commun.* **9**, 1129 (2018).
12. Wisitsorasak, A. & Wolynes, P. G. Dynamical heterogeneity of the glassy state. *J. Phys. Chem. B* **118**, 7835–7847 (2014).
13. Scalliet, C., Guiselin, B. & Berthier, L. Thirty milliseconds in the life of a supercooled liquid. *Phys. Rev. X* **12**, 041028 (2022).
14. Vila-Costa, A., Gonzalez-Silveira, M., Rodríguez-Tinoco, C., Rodríguez-López, M. & Rodriguez-Viejo, J. Emergence of equilibrated liquid regions within the glass. *Nat. Phys.* **19**, 114–119 (2023).
15. Kearns, K. L., Ediger, M. D., Huth, H. & Schick, C. One micrometer length scale controls kinetic stability of low-energy glasses. *J. Phys. Chem. Lett.* **1**, 388–392 (2010).
16. Rodríguez-Tinoco, C. et al. Surface-bulk interplay in vapor-deposited glasses: crossover length and the origin of front transformglasses with exceptional thermodynamic and kinetic stabilityation. *Phys. Rev. Lett.* **123**, 155501 (2019).
17. Vila-Costa, A. et al. Nucleation and growth of the supercooled liquid phase control glass transition in bulk ultrastable glasses. *Phys. Rev. Lett.* **124**, 076002 (2020).
18. Swallen, S. F. et al. Organic glasses with exceptional thermodynamic and kinetic stability. *Science* **315**, 353–356 (2007).
19. Ediger, M. D. Perspective: highly stable vapor-deposited glasses. *J. Chem. Phys.* **147**, 210901 (2017).
20. Rodriguez-Tinoco, C., Gonzalez-Silveira, M., Ramos, M. A. & Rodriguez-Viejo, J. Ultrastable glasses: new perspectives for an old problem. *La Riv. del. Nuovo Cim.* **45**, 325–406 (2022).
21. Queen, D. R., Liu, X., Karel, J., Metcalf, T. H. & Hellman, F. Excess specific heat in evaporated amorphous silicon. *Phys. Rev. Lett.* **110**, 135901 (2013).
22. Herrero, C., Scalliet, C., Ediger, M. D. & Berthier, L. Two-step devitrification of ultrastable glasses. *Proc. Natl Acad. Sci. U.S.A.* **120**, e2220824120 (2023).
23. Bowden, N., Brittain, S., Evans, A. G., Hutchinson, J. W. & Whitesides, G. M. Spontaneous formation of ordered structures in thin films of metals supported on an elastomeric polymer. *Nature* **393**, 146–149 (1998).
24. Chung, J. Y., Nolte, A. J. & Stafford, C. M. Surface wrinkling: a versatile platform for measuring thin-film properties. *Adv. Mater.* **23**, 349–368 (2011).
25. Cerda, E. & Mahadevan, L. Geometry and physics of wrinkling. *Phys. Rev. Lett.* **90**, 074302 (2003).
26. Yin, J., Cao, Z., Li, C., Sheinman, I. & Chen, X. Stress-driven buckling patterns in spheroidal core/shell structures. *Proc. Natl Acad. Sci. USA* **105**, 19132–19135 (2008).
27. Hoinka, N. M., Ostwald, C. & Fuhrmann-Lieker, T. Two-dimensional wrinkle resonators for random lasing in organic glasses. *Sci. Rep.* **10**, 2434 (2020).
28. Torres, J. M., Bakken, N., Li, J. & Vogt, B. D. Substrate temperature to control moduli and water uptake in thin films of vapor deposited *N,N'*-di(1-naphthyl)-*N,N'*-diphenyl-(1,1'-biphenyl)-4,4'-diamine (NPD). *J. Phys. Chem. B* **119**, 11928–11934 (2015).

29. Bakken, N., Torres, J. M., Li, J. & Vogt, B. D. Thickness dependent modulus of vacuum deposited organic molecular glasses for organic electronics applications. *Soft Matter* **7**, 7269 (2011).

30. Moon, M.-W. et al. Wrinkled hard skins on polymers created by focused ion beam. *Proc. Natl Acad. Sci. USA* **104**, 1130–1133 (2007).

31. Chung, J. Y., Nolte, A. J. & Stafford, C. M. Diffusion-controlled, self-organized growth of symmetric wrinkling patterns. *Adv. Mater.* **21**, 1358–1362 (2009).

32. Mondal, K., Liu, Y., Shay, T., Genzer, J. & Dickey, M. D. Application of a laser cutter to pattern wrinkles on polymer films. *ACS Appl. Polym. Mater.* **2**, 1848–1855 (2020).

33. Ràfols-Ribé, J. et al. Kinetic arrest of front transformation to gain access to the bulk glass transition in ultrathin films of vapour-deposited glasses. *Phys. Chem. Chem. Phys.* **20**, 29989–29995 (2018).

34. Vila-Costa, A., Gonzalez-Silveira, M., Rodríguez-Tinoco, C., Rodríguez-López, M. & Rodriguez-Viejo, J. Emergence of equilibrated liquid regions within the glass. *Nat. Phys.* **19**, 114–119 (2023).

35. Sepúlveda, A., Swallen, S. F. & Ediger, M. D. Manipulating the properties of stable organic glasses using kinetic facilitation. *J. Chem. Phys.* **138**, 12A517 (2013).

36. Mei, B., Zhuang, B., Lu, Y., An, L. & Wang, Z.-G. Local-average free volume correlates with dynamics in glass formers. *J. Phys. Chem. Lett.* **13**, 3957–3964 (2022).

37. Gao, S. & Simon, S. L. Measurement of the limiting fictive temperature over five decades of cooling and heating rates. *Thermochim. Acta* **603**, 123–127 (2015).

38. Rodríguez-Tinoco, C., Rams-Baron, M., Rodríguez-Viejo, J. & Paluch, M. Emergence of a substrate-temperature-dependent dielectric process in a prototypical vapor deposited hole-transport glass. *Sci. Rep.* **8**, 1380 (2018).

39. Das, A., Banerji, A. & Mukherjee, R. Programming feature size in the thermal wrinkling of metal polymer bilayer by modulating substrate viscoelasticity. *ACS Appl. Mater. Interfaces* **9**, 23255–23262 (2017).

40. Dalal, S. S., Walters, D. M., Lyubimov, I., de Pablo, J. J. & Ediger, M. D. Tunable molecular orientation and elevated thermal stability of vapor-deposited organic semiconductors. *Proc. Natl Acad. Sci. USA* **112**, 4227–4232 (2015).

41. Jin, Y. et al. Glasses denser than the supercooled liquid. *Proc. Natl Acad. Sci. USA* **118**, 1–7 (2021).

42. Jack, R. L. & Berthier, L. The melting of stable glasses is governed by nucleation-and-growth dynamics. *J. Chem. Phys.* **144**, 244506 (2016).

43. Zhang, Y. et al. Long-range correlated dynamics in ultra-thin molecular glass films. *J. Chem. Phys.* **145**, 114502 (2016).

Methods

Growth of organic glasses

Previous experiments have shown that capping a low T_g stable glass at both interfaces with a higher T_g material inhibits the formation of liquid fronts at its surfaces and interfaces forcing the glass to devitrify on heating through a bulk-like mechanism[16,17,33,35,44]. The stack we use in this work consists of trilayers of TCTA–TPD–TCTA grown on a rigid substrate (native SiO$_2$–Si) or bilayers of TCTA–TPD–rigid substrate with various TPD and TCTA thicknesses. TCTA has a glass transition temperature of 428 K (T_{g2}) and the T_g of TPD is 333 K (T_{g1}), so annealing above 333 K induces the transformation of the TPD while the TCTA remains as a rigid layer.

Thin-film glasses of TPD and TCTA were grown on both Si substrates and SiN$_x$ membranes at a substrate temperature of $0.85T_{g1}$ for TPD and $0.67T_{g2}$ for TCTA ($T_{sub} = 285$ K), to ensure TPD is formed as ultrastable glass. Since the TPD thickness is only around 65 nm, it is capped at both sides by an ultrathin layer of a TCTA layer of 13 nm. The growth rate is fixed at 0.08 nm s^{-1} for both materials. The trilayer structure is schematically shown in Fig. 1a (left). The kinetic and thermodynamic stability of the TPD layers is measured before and after capping with ultrathin layers of TCTA by in situ fast-scanning nanocalorimetry, as already shown elsewhere[44–46].

In operando AFM

Temperature-dependent AFM experiments were performed with a Keysight Technologies 5500 AFM controlled with a PicoScan 3000 electronics system, and enclosed in a chamber that was vibrationally and acoustically isolated[47]. Relative humidity was reduced below 10% relative humidity by circulating nitrogen. Heating was performed by gluing the samples with silver paste to a modified commercial high temperature stage from Keysight Technologies. The temperature was controlled with a LakeShore 311 Temperature Controller in a closed loop using the internal PT-100 sensor of the heater and measured with an additional PT-100 sensor glued with silver paste to the surface of the copper block of the heater (and close to the sample) and the resistance measured in a four-wire configuration. The temperature at the sample surface was periodically calibrated with an additional PT-100 sensor glued with silver paste on a silicon wafer of the same thickness as that of the samples. The x, y and z dimensions of the piezoscanner were calibrated with reference samples. For the 1×1 µm^2 scans, PS-PMMA block copolymers with fingerprint-like morphology and periods of 35 nm were used[48], while for larger scans (up to 20×20 µm^2) commercial calibration grating (TGXYZ01 and TGXYZ02 from MikroMasch) were used. Images were analysed with both WSxM[49] and Gwyddion[50].

The AFM was operated in open-loop intermittent contact mode using microfabricated silicon cantilevers with force constants of about 42 N m^{-1} and ultrasharp silicon tips (nominal tip radius $R < 10$ nm) (PPP-NCHR, Nanosensors). The resonance frequencies were in the 250–350 kHz range. After laser alignment, the sample was fixed to the heater and the heater stage coupled to the AFM head. When the whole setup was vibrationally and acoustically isolated, several images ranging from 1×1 up to 20×20 µm^2 in scan size were taken until stabilization of the microscope. Once stabilized at room temperature, the sample was withdrawn and the heater was driven up to T_{g1} −10 K at a heating rate of 5 K min^{-1} (as recommended by the manufacturer). Once the desired temperature was reached, the resonance frequency was tuned (the frequency decreases for increasing temperature), the laser was aligned again, the tip was engaged and a few images were acquired to check for the stability of the instrument. Then, the sample was withdrawn again and the temperature increased up to the target temperature, T_{g1} + 16 K. Again, when the temperature was reached, the tuning of the resonance frequency was not necessary in most cases to adjust the laser position. Then, the tip was engaged to find suitable regions to follow the isothermal evolution of the surface as a function of time. When the temperature experiments were finished, the sample was withdrawn, the

temperature control set to room temperature and after stabilization the resonance frequency was tuned, the laser position corrected and a few images at room temperature were acquired.

With the selected 512 points per line and two lines per second, each image took 256 s to complete (more than 4 min). Lower acquisition times were tested resulting in poor resolution images. Although shorter times would be highly desirable, the evolution of the features was slow enough to be tracked satisfactorily. During withdrawal and engage cycles, the tip would not land exactly on the same position (due to hysteresis of the piezoscanner), which makes it difficult to localize a specific region in transformed samples.

At the target temperature, the apparent lateral dimensions (for example, periodicity of the wrinkles) become smaller due to the increase of the strain coefficients (nm V^{-1}) of the piezoscanner with temperature that is not corrected during image acquisition[51]. The actual dimensions should be increased by a factor less than 10% (typically 5%), as obtained from images acquired at room temperature after the isothermal treatment. A similar trend is expected for the heights but in this case the correction is more involved since the tip–surface interaction should change with temperature, a behaviour that has not been explored sufficiently here, combined with the difficulty to localize a specific region at room temperature that was previously measured at high temperature, so that the obtained heights remain as apparent (uncorrected), although a 10% increase would be reasonable[51]. Further calibration experiments should be undertaken to quantify the variation of height with temperature. The spatial periodicity of the transformed surfaces has been calculated from the power spectral density (PSD) distribution as a function of the wavevector modulus[49]. In this case, the wavelength corresponds to the inverse of the wavevector (without the 2 π factor).

Finite element simulations

The thin-film system was modelled as an axisymmetric disc stiffened by the semi-infinite Si substrate (Supplementary Fig. 3). The overall thin-film geometry was discretized using 20-noded, brick-shape elements. Since possible processing stresses are unknown, the disc was assumed to be in the fully relaxed (or stress-free) configuration at the deposition temperature of 285 K. Linear thermoelasticity was then invoked as the temperature was ramped to 349 K in the first load step of the finite element simulations. This temperature was set in accordance with that where the surface corrugation occurred in the experiments. An inner disc of radius r representing the SCL region was then weakened in a second simulation stage, where numerical convergence was ensured after a slight temperature increment of 0.05 K. The finite element simulations were performed using ANSYS Multiphysics (release v.19.0, http://www.ansys.com).

The cylindrical, weakened SCL regions were assumed to deform in accordance with linear elasticity with specific Young's modulus E and Poisson's ratio v. Alternatively, the neo-Hookean hyperelastic formalism was also invoked so as to account for the potential decrease of the elastic modulus of the weakened SCL regions at small strains. In this model, the total strain energy density is given by $U = C(I_1 - 3) + d^{-1}(\det F - 1)^2$, where C and d are material parameters, I_1 is the first deviatoric strain invariant and $\det F$ is the volume ratio. The second term in the right-hand side of the neo-Hookean formulation explicitly accounts for possible material compressibility or volume changes, so that the SCL regions approach full incompressibility when $d \to 0$.

The capping TCTA top and bottom layers were assumed to remain linear elastic in all simulations, with matching Young's modulus E and Poisson ratio v to those in the glassy state (see the thermoelastic properties for the thin-film materials and Si substrate in Supplementary Information). The material parameters for the SCL disc where then allowed to vary within the wider ranges of $C = 3.84 \times 10^6$ to 1.43×10^7 Pa and $d = 1.12 \times 10^{-7}$ to 2.79×10^{-11} Pa^{-1}. The experimentally observed transition between the onset of a single ridge to wrinkles with increasing r

from 250 to 1,000 nm was then mimicked within the simulation subset where the SCL properties varied as before.

Data availability

Data that support the plots and other findings of this study are available at https://doi.org/10.5281/zenodo.7950765.

References

44. Leon-Gutierrez, E., Sepúlveda, A., Garcia, G., Clavaguera-Mora, M. T. & Rodríguez-Viejo, J. Stability of thin film glasses of toluene and ethylbenzene formed by vapor deposition: an in situ nanocalorimetric study. *Phys. Chem. Chem. Phys.* **12**, 14693–14698 (2010).

45. Leon-Gutierrez, E., Sepúlveda, A., Garcia, G., Clavaguera-Mora, M. T. & Rodríguez-Viejo, J. Correction: stability of thin film glasses of toluene and ethylbenzene formed by vapor deposition: an in situ nanocalorimetric study. *Phys. Chem. Chem. Phys.* **18**, 8244–8245 (2016).

46. Rodríguez-Tinoco, C. et al. Evaluation of growth front velocity in ultrastable glasses of indomethacin over a wide temperature interval. *J. Phys. Chem. B* **118**, 10795–10801 (2014).

47. Verdaguer, A., Cardellach, M. & Fraxedas, J. Thin water films grown at ambient conditions on BaF2(111) studied by scanning polarization force microscopy. *J. Chem. Phys.* **129**, 174705 (2008).

48. Fernández-Regúlez, M., Evangelio, L., Lorenzoni, M., Fraxedas, J. & Pérez-Murano, F. Sub-10 nm resistless nanolithography for directed self-assembly of block copolymers. *ACS Appl. Mater. Interfaces* **6**, 21596–21602 (2014).

49. Horcas, I. et al. A software for scanning probe microscopy and a tool for nanotechnology. *Rev. Sci. Instrum.* **78**, 013705 (2007).

50. Nečas, D. & Klapetek, P. Gwyddion: an open-source software for SPM data analysis. *Open Phys.* **10**, 181–188 (2012).

51. Ma, C., Chen, Y. & Huang, W. Environmental temperature effect on dimensional measurements of atomic force microscopy. *Nanotechnol. Precis. Eng.* **4**, 023003 (2021).

Author contributions

J.R.-V., C.R.-T. and M.G.-S. conceived the project. J.F., M.R.-R. and A.V.-C. performed the AFM experiments. T.B. performed the optical microscopy measurements. T.B., J.F. and M.R.-R. analysed the AFM and optical microscopy images. J.A.P. and J.A. contributed with the mechanical analysis and interpretation. C.R.-T., M.G.-S. and J.R.-V. discussed fundamental ideas of the transformation mechanisms. J.R.-V. wrote the manuscript with C.R.-T., J.F., J.A., J.A.P. and M.G.-S. All authors commented on the manuscript. J.R.-V. supervised the project.

Competing interests

The authors declare no competing interests.

Additional information

Supplementary information The online version contains supplementary material available at https://doi.org/10.1038/s41567-023-02125-0.

Correspondence and requests for materials should be addressed to Cristian Rodríguez-Tinoco or Javier Rodriguez-Viejo.

Peer review information *Nature Physics* thanks Heinz Sturm and the other, anonymous, reviewer(s) for their contribution to the peer review of this work.

Reprints and permissions information is available at www.nature.com/reprints.